Original Article

Utility of spectral CT with orthopedic metal artifact reduction algorithms for ^{125}I seeds implantation in mediastinal and hepatic tumors

Yuhan Zhou[1#^], Limin Lei[1#], Zhihao Wang[1], Weimeng Cao[1], Minghui Qin[1], Shushan Dong[2], Jinjin Dang[2], Zhigang Zhou[1]

[1]Department of Radiology, The First Affiliated Hospital of Zhengzhou University, Zhengzhou, China; [2]Department of Clinical Science, Philips Healthcare, Beijing, China

Contributions: Conception and design: Y Zhou; (II) Administrative support: Z Zhou; (III) Provision of study materials or patients: Y Zhou, Z Wang; (IV) Collection and assembly of data: Y Zhou, L Lei, Z Wang, W Cao; (V) Data analysis and interpretation: Y Zhou, L Lei; (VI) Manuscript writing: All authors; (VII) Final approval of manuscript: All authors.

[#]These authors contributed equally to this work.

Correspondence to: Zhigang Zhou, MD. Department of Radiology, the First Affiliated Hospital of Zhengzhou University, 1 Jianshe East Road, Zhengzhou 450052, China. Email: hnzzg126@126.com.

Background: Virtual monochromatic image (VMI) combined with orthopedic metal artifact reduction algorithms (VMI + O-MAR) can effectively reduce artifacts caused by metal implants of different types. Nevertheless, so far, no study has systematically evaluated the efficacy of VMI + O-MAR in reducing various types of metal artifacts induced by ^{125}I seeds. The aim of this study was to assess the effectiveness of combining spectral computed tomography (CT) images with O-MAR in reducing metal artifacts and improving the image quality affected by artifacts in patients after ^{125}I radioactive seeds implantation (RSI).

Methods: A total of 45 patients who underwent dual-layer detector spectral CT (DLCT; IQon, Philips Healthcare) scanning of mediastinal and hepatic tumors after ^{125}I RSI were retrospectively included. Spectral data were reconstructed into conventional image (CI), VMI, CI combined with O-MAR (CI + O-MAR), and VMI + O-MAR to evaluate the de-artifact effect and image quality improvement. Objective indicators included signal-to-noise ratio (SNR), contrast-to-noise ratio (CNR), and artifact index (AI) of lesions affected by artifacts. Subjective indicators included assessment of overcorrected artifacts and new artifacts, different morphology of artifacts, and overall image quality.

Results: In artifact-affected lesion areas, SNR and CNR in the CI/VMI + O-MAR groups were better than those in CI groups (all P values <0.05). The AI showed a downward trend as VMI keV increased (all P values <0.001). The AI values of the CI/VMI (50–150 keV) group were all higher than the groups of CI/VMI + O-MAR (50–150 keV) (P<0.001). Overcorrection artifacts and new artifacts were concentrated in the VMI50/70 keV groups. In the evaluation of artifact morphology, as the VMI keV increased, the number of near-field banding artifacts in hyperdense artifacts gradually decreased, whereas the number of minimal or no artifacts increased, and the total number of hyperdense artifacts were decreased. The diagnostic and image quality scores of hyperdense artifacts were higher than those of hypodense artifacts as VMI keV increased.

Conclusions: High VMI level combined with O-MAR substantially improve objective and subjective image quality, lesion display ability, and diagnostic confidence of CT follow-up after ^{125}I RSI, especially at the VMI + O-MAR 150 keV level.

^ ORCID: 0000-0002-3899-2485.

Keywords: Dual-layer spectral CT; ^{125}I radioactive seeds implantation (^{125}I RSI); virtual monochromatic image (VMI); orthopedic metal artifact reduction algorithms (O-MAR); image quality assessment

Submitted Jun 09, 2023. Accepted for publication Nov 08, 2023. Published online Jan 02, 2024.
doi: 10.21037/qims-23-843
View this article at: https://dx.doi.org/10.21037/qims-23-843

Introduction

In tumor radiotherapy, interstitial permanent brachytherapy (BT) has gradually become one of the primary techniques in radiotherapy. Due to the short radiation distance of ^{125}I seeds, it can provide more precise radiation doses to the tumor compared with external beam radiotherapy (EBRT), while applying the minimal radiation dose to adjacent normal tissues, thus improving patient tolerance and safety (1,2). Conventional computed tomography (CT) is the most commonly used non-invasive and repeatable examination for postoperative evaluation following ^{125}I seeds implantation which can effectively assess the displacement and re-distribution of the ^{125}I seeds (3). Meanwhile, according to the Response Evaluation Criteria in Solid Tumors (RECIST) score established by World Health Organization (WHO), conventional CT scans can be used to evaluate the maximum diameter of target lesions, degree of reduction of tumor necrosis areas (TNA), and surrounding lymph nodes (1,3-7). However, the hypo-/hyperdense artifacts produced by ^{125}I particle implantation severely affect the image quality and the evaluation of postoperative efficacy by covering the surrounding tissues. Metallic artifacts are severely affected by photon starvation and beam hardening effects, which significantly degrade the image quality of CT images. Photon starvation occurs due to the considerable absorption of low-energy photons by high-density and high-atomic-number metallic implants. This phenomenon leads to an increase in noise and loss of projection data, ultimately resulting in the formation of hypodense artifacts in reconstructed images (8). Beam-hardening artifacts are caused by a phenomenon in which the high density and high atomic number of metallic objects cause the absorption of a significant number of low-energy photons when exposed to X-rays (9).

In recent years, virtual monoenergetic image (VMI) has achieved a substantial reduction in beam-hardening artifacts by reconstructing high VMI level images, minimizing the absorption of low-energy photons by metallic objects. Simultaneously, orthopedic metal artifact reduction algorithms (O-MAR) could partially correct photon starvation artifacts by modifying both the projection and image data of conventional CT scans (10-13). More importantly, multiple studies have shown that VMI combined with O-MAR can effectively reduce the photon starvation and beam-hardening artifacts caused by metal implants of different types, and hypodense artifacts are predominantly caused by photon starvation (14-16). The purpose of this study was to investigate the potential of dual-layer detector spectral CT (DLCT)-derived VMI and O-MAR reconstructions as their combination (VMI + O-MAR) for metal artifact reduction and improvement of image quality in patients who underwent ^{125}I seeds implantation. We present this article in accordance with the STROBE reporting checklist (available at https://qims.amegroups.com/article/view/10.21037/qims-23-843/rc).

Methods

Patient population

This retrospective study was conducted in accordance with the Declaration of Helsinki (as revised in 2013) and approved by the Institutional Review Board of The First Affiliated Hospital of Zhengzhou University (No. 2022-KY-1396). Individual consent for this retrospective analysis was waived. The study involved 52 postoperative patients who had undergone ^{125}I seeds implantation at the First Affiliated Hospital of Zhengzhou University between September 2022 and January 2023. The ^{125}I seeds were made up of cylindrical entities with a diameter of 0.8 mm and a length of 4.5 mm, encased in titanium metal. The average number of ^{125}I seeds was 25.5 (range, 10 to 35). The inclusion criteria were as follows: (I) patients who had undergone ^{125}I seeds implantation for thoracic and liver tumors and required follow-up DLCT scans; (II) age of 18 years or above; (III) body mass index (BMI) <28 kg/m^2. The exclusion criteria were as follows: (I) allergic reactions to iodinated contrast agents; (II) presence of other metal implants in addition to ^{125}I particles in the patient's body;

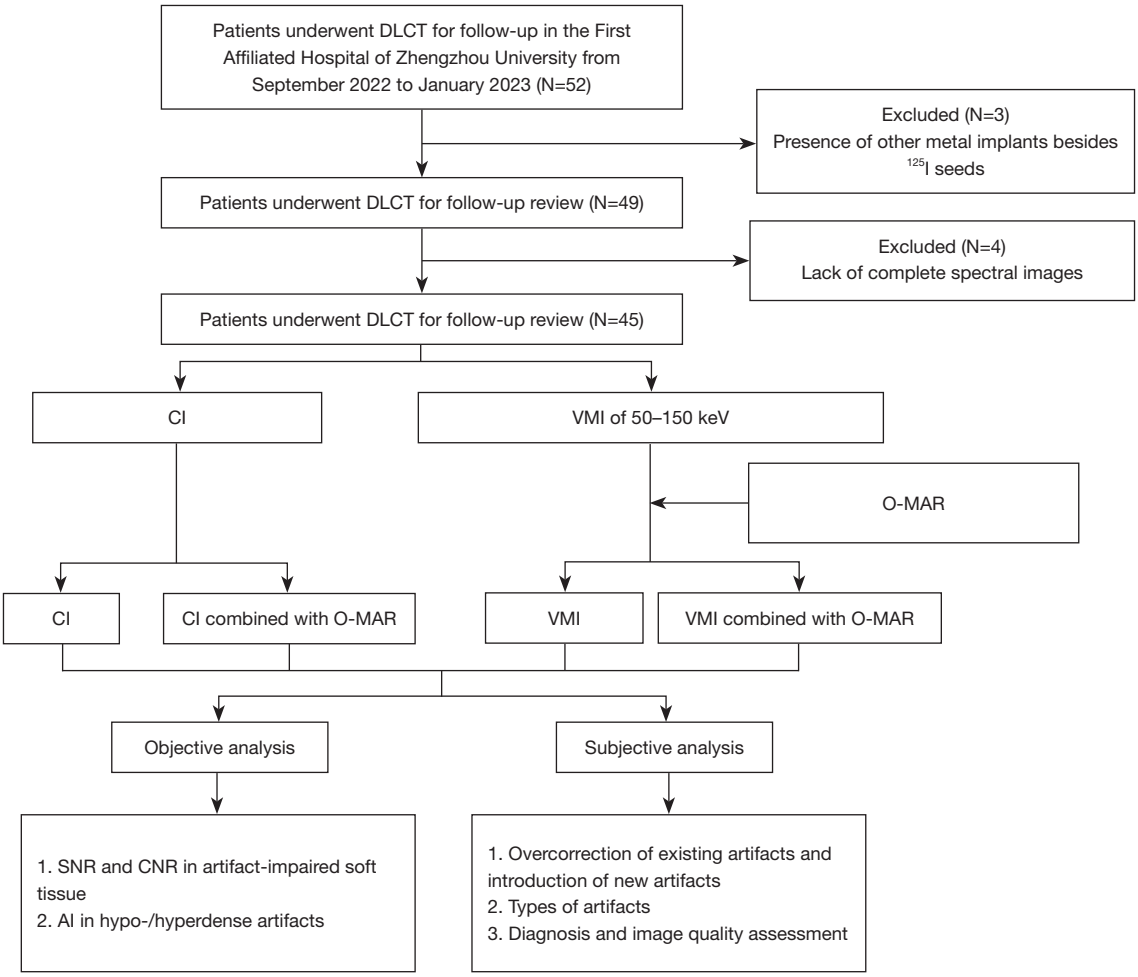

Figure 1 Workflow of the experimental design: group and metal artifacts evaluation indicators. DLCT, dual-layer detector spectral CT; CI, conventional image; VMI, virtual monochromatic image; O-MAR, orthopedic metal artifact reduction algorithms; SNR, signal-to-noise ratio; CNR, contrast-to-noise ratio; AI, artifact index; CT, computed tomography.

(III) incomplete or missing CT images. The workflow of the experimental design is depicted in *Figure 1*, which shows the flow chart of the population selection. Finally, a total of 45 patients were available for our final analysis, including 24 males and 21 females. The mean age of the participants was 57.5±10.54 years, ranging from 23 to 80 years. Among them, there were 10 cases of mediastinal tumors, 12 cases of hepatocellular carcinoma, 6 cases of cholangiocarcinoma, and 17 cases of liver metastatic tumors. For each patient, the slice with the most significant artifact was selected for assessment, resulting in a total of 45 slices.

Image acquisition and reconstruction

DLCT (IQon; Philips Healthcare, Andover, MA, USA) was used to perform helical scans of the chest and upper abdomen. The patients were directed to lie on their backs, and the scanning range covered from the lung apex to the lower edge of the liver. The scanning parameters were as follows: tube voltage 120 kV, automatic tube current technology (100–350 mAs), pitch ratio 1:1, rotation time 0.5 s, slice thickness 1 mm, interlayer spacing 1 mm, matrix size 512×512, and a dose right index of 20. The reconstruction parameters used were iDose^4, level 4. After the non-contrast CT scan, iodinated contrast agent iohexol (350 mgI/mL) at a dose of 1.2 mL/kg was injected via the right antecubital vein with a dual-chamber high-pressure injector at a flow rate of 3 mL/s, followed by 20 mL of saline. Using a threshold value of 150 Hounsfield units (HU) set at the descending aorta, arterial phase initialization

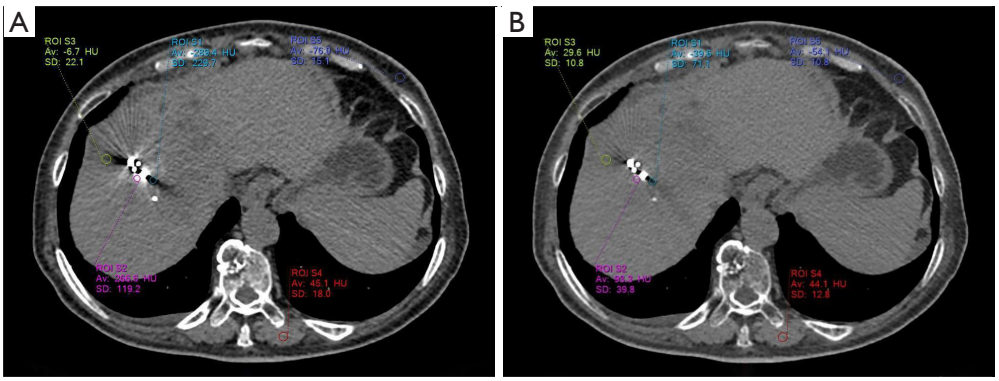

Figure 2 A schematic diagram of ROI delineation. (A) CI; (B) VMI + O-MAR 150 keV image. ROI S1 represents the hypodense artifacts (ROI_L); ROI S2 represents the hyperdense artifacts (ROI_H); ROI S3 represents the soft tissue affected by metal artifacts (ROI_T); ROI S4 represents the same slice of vertebral muscle (ROI_M); ROI S5 represents the same slice of adipose tissue regions (ROI_A). VMI, virtual monochromatic image; O-MAR, orthopedic metal artifact reduction algorithms; ROI, regions of interest; CT, computed tomography; CI, conventional image.

acquisition was performed 12 seconds after triggering, and portal venous phase image acquisition was performed 30 seconds after arterial phase image acquisition.

The original data were imported to post-processing workstation (Intellispace Portal, Philips Healthcare) to generate spectral-based images (SBIs) with and without the O-MAR algorithm (8). Then the SBIs were divided into conventional image (CI), VMI with 6 levels of 50, 70, 90, 110, 130, and 150 keV, CI combined with O-MAR (CI + O-MAR), and VMI combined with O-MAR (VMI + O-MAR). We selected the VMI reconstruction range of 50–150 keV to assess the effectiveness of each energy level in VMI images and the impact of fusion with O-MAR in artifact reduction as multiple studies had indicated that the optimal VMI level range for reducing artifacts was between 70–140 keV (9). For all sets of reconstructed CT images for each patient, the slice with the most prominent artifacts was selected to assess image quality and the effectiveness of artifact removal.

Objective analysis

Objective and subjective evaluation of images was performed on post-processing workstation (Intellispace Portal, Philips Healthcare) non-enhanced images were used for objective analysis. For each patient, the slice with the most significant artifact was selected for assessment. In the images of CI groups, regions of interest (ROI) ranging from 15 to 30 mm^2 were respectively placed in the area of most pronounced hypoattenuating artifact (ROI_L), the most pronounced hyperattenuating artifact (ROI_H), and the soft tissue areas affected by artifacts (ROI_T). ROI_T that were partially covered by the artifacts but partially visible outside the range of 1 cm adjacent to the metal, the left vertebral muscle (ROI_M), and adipose tissue regions (ROI_A) of the same slice were selected. Then, all ROIs were copied to the corresponding slices of the VMI, CI + O-MAR, and VMI + O-MAR images (*Figure 2*). The CT value and standard deviation (SD) of each ROI area were measured and recorded and the signal-to-noise ratio (SNR) of the soft-tissue region affected by artifacts on the same layer was calculated using the formula $SNR=CT_T/SD_T$. The contrast-to-noise ratio (CNR) was calculated using the formula $CNR=|CT_T - CT_A|/(SD_T^2 + SD_A^2)^{1/2}$. The artifact index (AI) of hypo-/hyperdense artifacts was calculated using the formula $AI=(SD_{L/H}^2 - SD_M^2)^{1/2}$ (17). The SNR and CNR were used to assess the image quality of the soft tissue areas affected by artifacts and the AI was used to evaluate the intensity of the artifacts (17).

Subjective analysis

The subjective evaluation was performed by 2 radiologists with over 5 years of experience in tumor imaging, and the reconstruction method and grouping were hidden during the evaluation process. Meanwhile, we utilized venous phase images for subjective analysis. Both radiologists received training before the qualitative evaluation: the 2 radiologists blindly evaluated the overcorrection of artifacts and the occurrence of new artifacts, types of artifacts, and the

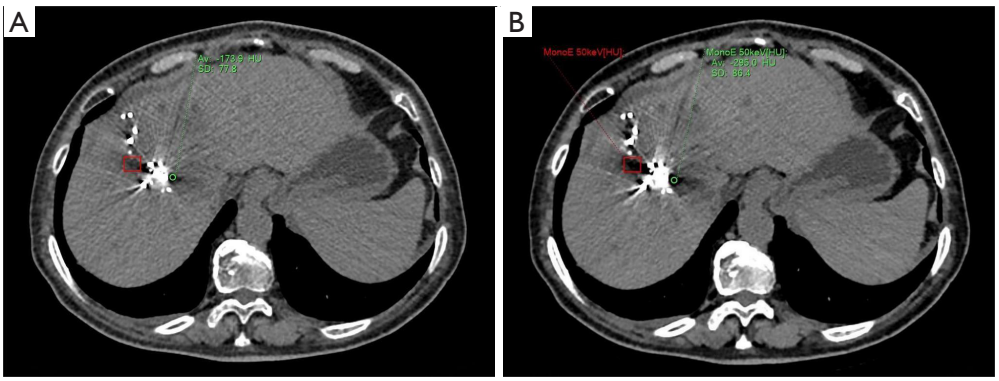

Figure 3 A schematic diagram of ROI delineation. (A) CI image; (B) VMI + O-MAR 50 keV image. The green circular region represents overcorrection of existing artifacts, the red rectangular region represents the new artifacts. Compared with the HU and SD values of the green circular area in (A), the HU and SD values in (B) are significantly enhanced. VMI, virtual monochromatic image; O-MAR, orthopedic metal artifact reduction algorithms; ROI, regions of interest; CT, computed tomography; CI, conventional image; HU, Hounsfield unit; SD, standard deviation.

diagnostic and image quality scores in a random selection of 12 sets of images. In case of any discrepancies, the 2 radiologists reached a consensus through discussion. After 2 weeks, a formal evaluation was conducted on the images with hidden reconstruction methods and groups, and the dataset utilized for training also underwent a reassessment. A 2-point system was used to evaluate whether there was excessive correction or new artifacts in the images: 0 points for images without overcorrection of existing artifacts/new artifacts, and 1 point for images with overcorrection of existing artifacts/new artifacts (*Figure 3*). The overcorrection of existing artifacts was interpreted as the artifacts that were significantly enhanced in the position of the original artifacts in the CI images. The new artifacts were areas that were not present on CI images, accompanied by a significant increase in severe artifact area. Metal artifacts caused by ^{125}I seeds implantation were classified into 5 categories: type a, near-field banding artifact; type b, near-field streak artifact; type c, far-field streak artifact; type d, blurred artifact; type e, minimal or no artifacts (*Figure 4*). Type a: near-field banding artifacts: wide artifacts of completely covered tissue around ^{125}I seeds. Type b: near-field streak artifacts: narrow artifacts of completely covered tissue around ^{125}I seeds. Type c: far-field streak artifacts: The artifacts with long distance and partially covered tissue. Type d: blurred artifacts: The artifacts of partially covered tissue around ^{125}I seeds. Type e: minimal or no artifacts: The artifact were extremely short and not affecting the tissue around ^{125}I seeds, or no artifacts. The existence and number of various types of artifacts in different reconstructed images were recorded. The types of hypo-/hyperdense artifacts in each group and total number of different types of artifacts were evaluated. The image quality scores affected by the artifacts were evaluated using a 5-point system in accordance with the RECIST: 5, image quality can completely meet diagnostic requirements, clear boundaries of ^{125}I seeds, and clearly measurable lesion long axis with distinguishable tissue borders, and necrotic tissue; 4, the diagnostic efficacy was not affected by minor artifacts/minor artifacts affected the diagnostic efficacy but the ^{125}I seeds boundaries were still recognizable, with a measurable lesion long axis, partially clear tissue borders, and necrotic tissue; 3, despite the presence of artifacts, the image remained suitable for diagnosis but showed slightly blurry ^{125}I seeds particle edges, a partially measurable lesion long axis, some affected border visibility of adjacent tissues, and necrotic areas were still recognizable; 2, restricted diagnosis. The boundaries of ^{125}I seeds were unclear in the image, the lesion long axis was unmeasurable, the border visibility of adjacent tissues was affected, and necrotic areas showed uneven density radiating from the artifacts with fuzzy recognition; 1, complete failure of diagnosis, fusion of metal particles with artifacts, unmeasurable lesion long axis, affected border visibility of adjacent tissues, and necrotic areas completely covered by artifacts. During the evaluation process, modifying window settings and using multi-planar reconstruction were allowed. A soft tissue window with a width of 60 and a level of 360 was selected for axial image diagnosis.

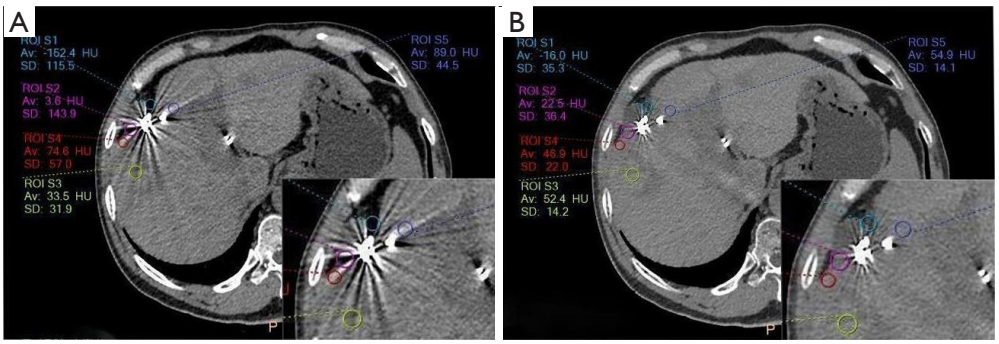

Figure 4 A 48-year-old male who received hepatic tumor ^{125}I seeds implantation 1 year ago and underwent DLCT examination after 1 month. (A) CI, the ROI for the different types of artifacts observed, including: S1, hypodense near-field banding artifacts of type a; S2, hypo-/hyperdense near-field streak artifacts of type b; S3, hypodense far-field streak artifact of type c; S4 and S5, hyperdense blurred artifact of type d. (B) VMI + O-MAR 150 keV image, the ROIs for the different types of artifacts observed, including: S1 and S2, hypo-/hyperdense near-field streak artifacts of type b; S3–S5, minimal or no artifacts of type e. The implementation of higher VMI keV level in combination with O-MAR showed improvement in correcting the morphology and quantifying the number of artifacts, compared to CI image. VMI, virtual monochromatic image; O-MAR, orthopedic metal artifact reduction algorithms; DLCT, dual-layer detector spectral computed tomography; ROIs, regions of interest; CT, computed tomography; CI, conventional image.

Statistical analysis

The software SPSS 25.0 (IBM Corp., Armonk, NY, USA) was used for statistical analysis. Shapiro-Wilk test was used to test the normality of counting data. The one-way analysis of variance (ANOVA) was used for multiple data with normal distributions, and Bonferroni test (uniform variance) or Tamhane's test (uneven variance) was used for the post-hoc comparisons. The Kruskal-Wallis test was used for quantitative data without normal distributions. Paired *t*-test was used for the comparation between the CI/VMI groups and the corresponding CI/VMI + O-MAR groups. The kappa test was used to test the consistency of subjective evaluation of hypo-/hyperdense artifacts between observers: Kappa <0.2 indicated poor consistency, 0.2–0.4 indicated general consistency, 0.4–0.6 indicated moderate consistency, 0.6–0.8 indicated strong consistency, and 0.8–1.0 indicated very strong consistency. A 2-tailed P value <0.05 was considered statistically significant.

Results

Objective analysis

The Shapiro-Wilk test revealed that the numerical values of all quantitative parameters (CNR, SNR, AI) followed a normal distribution (all P>0.05). A significant statistical difference was observed in the SNR values among the various groups in ROI_T artifacts (P<0.001). Post hoc comparisons indicated that the SNR of the VMI + O-MAR (110–150 keV) group was significantly higher than that of the CI group (P values were 0.017, 0.007, and 0.004, respectively), whereas there was no statistically significant difference among the other groups. The comparison between the CI group and the CI + O-MAR group, as well as between the VMI group and the VMI + O-MAR group, was represented as CI/VMI versus CI/VMI + O-MAR. The paired *t*-test conducted between CI/VMI (50–150 keV) and CI/VMI + O-MAR (50–150 keV) groups revealed that the SNR of the CI/VMI + O-MAR (70–150 keV) group was significantly higher than that of the CI/VMI (70–150 keV) group (P values were: 0.003, 0.022, 0.008, <0.001, <0.001, <0.001, respectively). These results are presented in *Table 1*.

There was a statistically significant difference in CNR values among the groups (P<0.001), post hoc testing comparisons revealed that the CNR values of the VMI + O-MAR (90–150 keV) group were significantly higher than those of the CI group (P values were 0.021, 0.008, 0.005, and 0.005, respectively). In comparing different CI groups, the CNR of each CI/VMI + O-MAR (50–150 keV) group was significantly higher than that of the CI group (P<0.001), as demonstrated in *Table 1*. In addition, the SNR values of the CI/VMI + O-MAR (50–150 keV) groups were all greater than those of the CI/VMI (50–150 keV) group (P<0.001), as shown in *Table 1*.

In the $ROI_{H/L}$ hypo-/hyperdense artifacts, as the VMI keV increased in each group of CI/VMI (50–150 keV) and

Table 1 Paired *t*-tests of SNR and CNR between CI/VMI groups and CI/VMI + O-MAR groups

SNR and CNR	CI	VMI					
		50 keV	70keV	90 keV	110 keV	130 keV	150 keV
SNR							
CI	2.44±0.87	2.29±1.00	2.42±0.81	2.55±0.90	2.6±0.96	2.63±1.00	2.64±1.03
O-MAR	2.82±1.40	2.39±1.12	2.68±1.17	2.88±1.26	3.03±1.39	3.11±1.47	3.15±1.51
P value	0.003	0.541	0.022	0.008	<0.001	<0.001	<0.001
CNR							
CI	4.33±1.46	3.87±1.68	4.19±1.42	4.41±1.66	4.63±1.62	4.72±1.67	4.76±1.70
O-MAR	6.16±2.20	5.18±2.22	5.5±1.98	5.76±2.03	5.95±2.18	6.03±2.26	6.06±2.29
P value	<0.001	<0.001	<0.001	<0.001	<0.001	<0.001	<0.001

Data represented as mean ± standard deviations. SNR, signal-to-noise ratio; CNR, contrast-to-noise ratio; CI, conventional image; VMI, virtual monochromatic image; O-MAR, orthopedic metal artifact reduction algorithms.

CI/VMI + O-MAR (50–150 keV), the AI values showed a decreasing trend, and the differences were statistically significant (P<0.001). Furthermore, in the hypo-/hyperdense artifacts, the AI values of the CI/VMI (50–150 keV) group were all higher than those of the corresponding groups of CI/VMI + O-MAR (50–150 keV) (P<0.001), as shown in *Table 2*. A small number of outliers were shown in objective indicator measurement and calculation, which might be related to the dispersion or clustering of the ^{125}I seeds caused by tumor necrosis and almost not affecting the results.

Subjective analysis

Overcorrection of existing artifacts and new artifacts in each group of VMI (50–150 keV), CI + O-MAR, and VMI + O-MAR (50–150 keV) are shown in *Table 3*. The total number of overcorrected existing artifacts and new artifacts in the VMI + O-MAR groups were less than that in the groups without O-MAR. In the groups without the O-MAR algorithm, all the overcorrection of existing artifacts and new artifacts were generated by the VMI + O-MAR 50 and 70 keV groups. In the groups with O-MAR, 100% of overcorrection of existing artifacts and 89.8% of new artifacts were generated by the VMI + O-MAR 50 and 70 keV groups.

The changes in the different types of hypo-/hyperdense artifacts in different groups of CI/VMI (50–150 keV) and CI/VMI + O-MAR (50–150 keV) are compared in *Figure 5*. As the VMI keV increased, there was a gradual reduction in the number of a-type banding artifacts observed in hyperdense artifacts, whereas the number of e-type minimal or no artifacts increased compared to hypodense artifacts. Furthermore, the total number of hyperdense artifacts of each type showed a decreasing trend with the increase of VMI keV, and the hyperdense artifacts of all types significantly decreased compared to the number of hypodense artifacts. *Figure 2A* depicts a post-^{125}I seeds implantation CI image, shown a-type banding artifacts, b-type near-field streak artifacts, c-type far-field streak artifacts, and d-type blurred artifacts. *Figure 2B* illustrates the postoperative VMI + O-MAR150 keV image of the same patient, shown d-type blurred artifacts and e-type minimal or no artifacts.

In the image quality assessment of tissue affected by artifacts, as the VMI keV increased, the subjective evaluation scores of diagnosis and image quality of hypo-/hyperdense artifact region in the VMI + O-MAR (50–150 keV) group showed an increasing trend. Comparing the CI/VMI (50–150 keV) and CI/VMI + O-MAR (50–150 keV) groups, the image quality scores of CI/VMI + O-MAR (50–150 keV) were higher in each VMI keV level. Meanwhile, in the comparisons between hypo-/hyperdense artifacts among the different VMI keV groups, there were significant differences in both the image quality scores for each VMI keV level both in hypo-/hyperdense artifacts between the CI/VMI and CI/VMI + O-MAR groups (P<0.05), as shown in *Figure 6*, with kappa values of 0.63 and 0.70, respectively, for hypo-/hyperdense artifacts.

Discussion

This study systematically evaluated the correction value

Table 2 Paired *t*-tests of $AI_{low/high}$ between CI/VMI groups and CI/VMI + O-MAR groups

AI	CI	VMI					
		50 keV	70 keV	90 keV	110 keV	130 keV	150 keV
AI_{Low}							
CI	102.00±48.26	171.29±69.32	99..09±49.26	71.24±33.62	58.43±28.62	50.72±22.79	44.36±18.83
O-MAR	50.05±28.36	105.48±49.33	58.42±22.63	45.03±24.28	33.45±20.64	31.54±15.38	28.64±14.28
P value	<0.001	<0.001	<0.001	<0.001	<0.001	<0.001	<0.001
AI_{High}							
CI	78.64±28.32	144.48±50.75	78.32±32.86	54.97±22.48	44.72±20.27	39.24±14.05	36.72±15.05
O-MAR	38.48±21.83	85.97±50.62	45.85±25.40	33.72±19.08	26.90±15.86	24.58±15.36	20.89±12.45
P value	<0.001	<0.001	<0.001	<0.001	<0.001	<0.001	<0.001

Data represented as mean ± standard deviations. AI_{low}, artifact index of hypodense artifacts; AI_{High}, artifact index of hyperdense artifacts; CI, conventional image; VMI, virtual monochromatic image; O-MAR, orthopedic metal artifact reduction algorithms.

Table 3 Overcorrection of existing artifacts and introduction of new artifacts

Variables	Overcorrection of existing artifacts, n (%)	Introduction of new artifacts, n (%)
CI + O-MAR		
50 keV	43 (68.2)	38 (77.6)
70 keV	20 (31.7)	11 (22.4)
90 keV	0	0
110 keV	0	0
130 keV	0	0
150 keV	0	0
Total	63 (100.0)	49 (100.0)
O-MAR and VMI + O-MAR		
O-MAR	0	1 (2.6)
50 keV O-MAR	38 (77.6)	29 (74.4)
70 keV O-MAR	11 (22.4)	6 (15.4)
90 keV O-MAR	0	1 (2.6)
110 keV O-MAR	0	1 (2.6)
130 keV O-MAR	0	1 (2.6)
150 keV O-MAR	0	0
Total	49 (100.0)	39 (100.0)

Overcorrection of existing artifacts and introduction of new artifacts were expressed in the number of cases; with the percentage of overcorrection artifacts and new artifacts to the total number of cases in parentheses. CI, conventional image; VMI, virtual monochromatic image; O-MAR, orthopedic metal artifact reduction; VMI + O-MAR, virtual monochromatic image combined with metal artifact reduction algorithms.

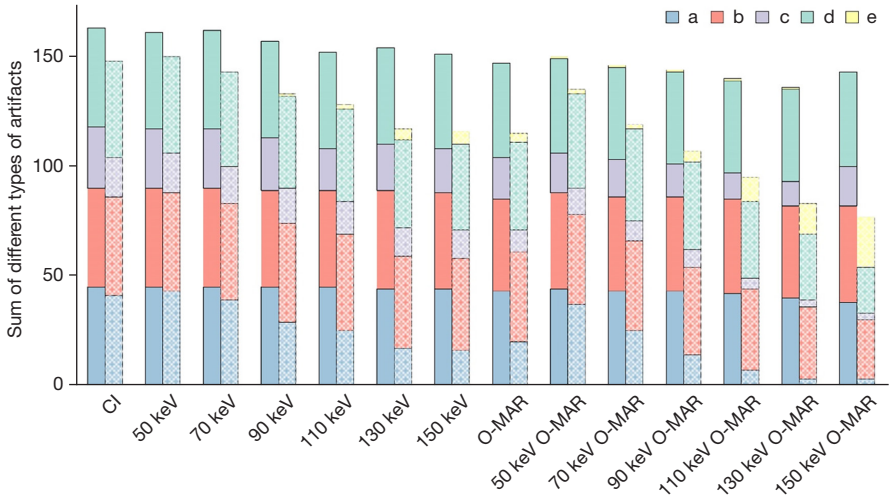

Figure 5 The various forms of artifacts utilized clustered stacked bar charts to illustrate: a, near-field banding artifacts (blue); b, near-field streak artifact (red); c, far-field streak artifact (purple); d, blurred artifact (green); e, minimal or no artifacts (yellow). The X-axis represents the groups of CI + VMI (50–150 keV) and CI + VMI (50–150 keV) + O-MAR. To facilitate a clear comparison between the hypo-/hyperdense artifacts, each form of artifacts is presented in a paired stacked bar chart. The left side displays the total number and proportion of hypodense artifacts, while the right side shows the total number and proportion of hyperdense artifacts for each form. CT, computed tomography; CI, conventional image; VMI, virtual monochromatic image; O-MAR, orthopedic metal artifact reduction algorithms.

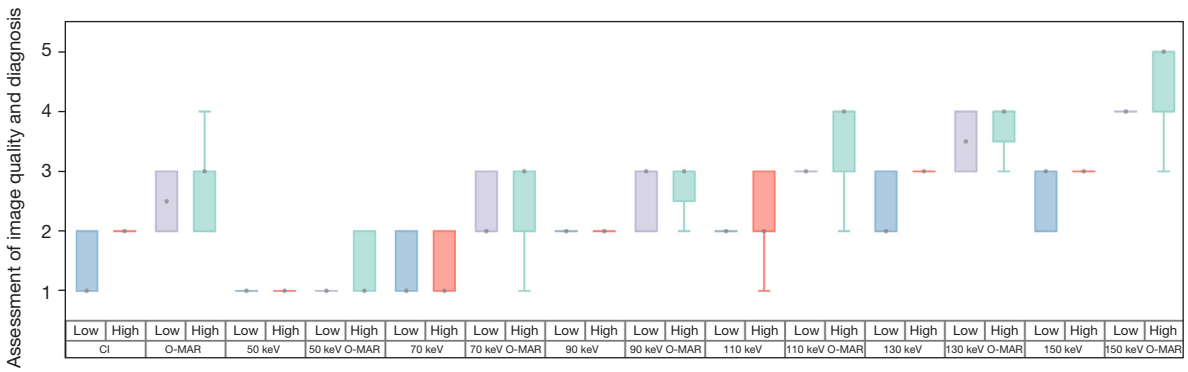

Figure 6 The multi-factor group box plot provides a visual representation of the subjective scores for image quality in hypo-/hyperdense artifacts for each group. The X-axis is divided into two sections: The first row representing the subgroup of hypo-/hyperdense artifacts in each group. The second row representing the CI/VMI and O-MAR groups. The CI/VMI group's hypodense artifact affected regions are denoted in blue, the hyperdense artifact affected regions are shown in red. Similarly, the hypodense artifact affected regions in the CI/VMI + O-MAR groups are represented in purple, and the hyperdense artifact affected regions are shown in green. CI, conventional image; VMI, virtual monochromatic image; O-MAR, orthopedic metal artifact reduction algorithms.

of spectral VMI images combined with O-MAR for different types and morphologies of metallic artifacts and investigated its application in the postoperative follow-up of ^{125}I particle implantation in patients with mediastinal and hepatic tumors. In the objective assessment, the SNR and CNR of higher VMI keV level combined with O-MAR were significantly improved compared to the CI images, whereas AI was significantly reduced. In the subjective assessment, the number of hypo-/hyperdense type-a artifacts significantly decreased, and the number of type-e artifacts significantly increased with higher VMI keV level combined with O-MAR. This effect was particularly pronounced in hyperdense artifacts. In terms of diagnosis and image quality evaluation of tissues affected by artifacts,

the reduction of high-density artifacts in higher VMI keV level combined with O-MAR images was particularly significant.

Our study showed that increasing VMI keV led to an increasing trend in both SNR and CNR for ^{125}I seed implantation, both SNR and CNR of the CI/VMI + O-MAR (110–150 keV) was significantly higher than that of the CI group using post hoc (P<0.05), and the CI/VMI + O-MAR (70–150 keV) group was significantly higher than that of the CI/VMI (70–150 keV) group using paired *t*-test (P<0.05), particularly in the VMI + O-MAR 150 keV group. These findings suggested a marked improvement in the objective image quality of follow-up CT examination for patients who underwent ^{125}I seeds implantation using VMI + O-MAR 150 keV. Possibly, this was due to high VMI levels' synergistic effect on beam hardening artifacts and O-MAR's collaboration on photon starvation mitigation. In assessing image quality related to metal artifact reduction, SNR and CNR are common parameters used to objectively evaluate the quality of the reconstructed images. A study involving a bone implant model demonstrated that VMI combined with O-MAR significantly improved the SNR of images compared to the VMI groups. The best artifact reduction effect for orthopedic metal implantation was observed when using VMI + O-MAR at 140 keV (17). Another study revealed that VMI combined with MAR significantly increased the CNR of images following ^{125}I seeds implantation. The optimal SNR and CNR values were achieved at VMI 80 keV(4). The disparity between the optimal VMI keV level in our study and previous literature suggested significant differences in the spectral imaging methods utilized in the 2 studies. In our study, the spectral imaging principle was based on energy CT imaging utilizing a dual-layer detector, whereas earlier research employed rapid kVp switching. A phantom study based on various spectral imaging methods demonstrated that in energy imaging with kVp switching, the background noise of VMI keV may exhibit significant fluctuations with changes in keV, particularly in the range of 70–90 VMI keV. In contrast, background noise remains stable in energy CT imaging based on a dual-layer detector. This discrepancy might give rise to variations in the optimal single-energy level across different spectral imaging platforms (18).

AI is mainly related to the average CT value of the background noise and artifact regions and is an independent indicator for evaluating artifact load (17). In our study, both hypo-/hyperdense artifacts observed in the VMI and VMI-O + MAR groups exhibited a decreasing trend with increasing VMI keV. Compared with the VMI group at each VMI keV level, the VMI + O-MAR groups had significantly reduced artifacts (P<0.001). This indicates that VMI combined with O-MAR can further reduce the AI, leading to an enhancement in image quality of the artifact coverage regions beyond what can be achieved with VMI alone. VMI combined with O-MAR has been shown to be effective for joint metal implants, intracranial arterial embolization coils, and oral metal implants (19-22). A previous study indicated that the AI value initially increased and then decreased as VMI keV increased. The lowest AI value was achieved at a virtual monoenergetic level of 80 keV (4). Another study focused on artifact reduction after ^{125}I seeds implantation revealed that the average SD value and AI value of artifact images decreased as VMI keV increased (3). In line with earlier research findings, this could be attributed to the synergistic effect of VMI in reducing beam hardening artifacts and O-MAR in mitigating photon starvation effects.

In subjective image evaluation, our study found that overcorrection artifacts and new artifacts were predominantly observed in the VMI 50–70 keV range. The occurrence rates of overcorrection and new artifacts in other VMI keV levels were significantly reduced. Overcorrection of existing artifacts and new artifacts have been reported in several studies (23,24). A previous study showed that the metal artifact reduction reconstruction algorithm (MAR) in dental implant research, overcorrection of existing artifacts, and new artifacts were observed at each VMI keV level (22). This might reflect the amplification effect of scatter noise under low VMI keV, resulting in increased intensity and area of hypo-/hyperdense artifacts (22). Meanwhile, compared to the VMI 50–70 keV groups, the VMI + O-MAR 50–70 keV groups had lower rates of overcorrection artifacts and new artifacts. This indicated that O-MAR might correct the overcorrection artifacts and new artifacts caused by low VMI keV. Therefore, it indicated that VMI below 70 keV was not suitable for metal artifact reduction. Our work showed that VMI combined with O-MAR exhibited a better artifact reduction effect at higher VMI keV levels and was less prone to producing new artifacts.

Metal artifacts lead to a combination of factors, including photon starvation, beam hardening, scattering, noise, and edge effects (9). These factors collectively contribute to the generation of various types and densities of artifacts. Several studies have revealed that the shapes and intensities of metal artifacts can be altered by utilizing different artifact

reduction algorithms (3). Furthermore, hypodense artifacts are caused by photon starvation, wherein high-density and high atomic number metallic implants lead to the absorption of a significant number of low-energy photons, preventing these photons from reaching the detector. Meanwhile, hyperdense artifacts are caused by beam hardening, which causes greater attenuation of low-energy photons compared to photons with higher energy (24). Our study showed that in comparison to hypodense artifacts, the number of a-type hyperdense artifacts decreased with increasing VMI keV, whereas the number of e-type hyperdense artifacts gradually increased in higher VMI keV. More importantly, the occurrence of various forms of hyperdense artifacts was significantly lower in the VMI + O-MAR 150 keV group, and in image quality evaluations, subjective scores related to areas affected by hyperdense artifacts were higher than those affected by hypodense artifacts. These findings indicate that VMI combined with O-MAR had a superior correction effect on these hyperdense artifacts, and could be associated with the substantial correction effect of higher energy VMI keV on high-density artifacts induced by beam hardening (15). Meanwhile, our study revealed that in the VMI + O-MAR (50–150 keV) group, the subjective scores of areas affected by hypo-/hyperdense artifacts exhibited an increasing trend with the increment of VMI keV; this might be related to the synergistic interplay between O-MAR further correcting photon-starvation artifacts and the correction of beam-hardening artifacts through higher-energy VMI keV.

This study had some limitations. Firstly, the relatively small sample size, which may have impacted the statistical distribution of certain data. Secondly, during patient follow-up, the clustering of ^{125}I seeds caused by tumor necrosis and changes in ^{125}I seed displacement and distribution might be related to the intensity of metal artifacts, and this phenomenon might have led to a minor number of outliers. Further investigations are required to better understand the potential impact of changes in ^{125}I seeds displacement and distribution on metal artifacts during patient follow-up. Thirdly, it is worth noting that this study only utilized axial images to evaluate metal artifacts. It is essential that radiologists should evaluate the clarity of particle borders and distribution using coronal/sagittal images in addition to axial images.

Conclusions

Our study suggested that higher VMI keV level combined with O-MAR resulted in a significant improvement in CT image quality, particle distribution, and lesion display ability during follow-up CT examination in patients who underwent ^{125}I seeds implantation. It was particularly notable at the VMI + O-MAR150 keV level. A large-scale prospective study is needed to substantiate our findings.

Acknowledgments

Funding: None.

Footnote

Reporting Checklist: The authors have completed the STROBE reporting checklist. Available at https://qims.amegroups.com/article/view/10.21037/qims-23-843/rc

Conflicts of Interest: All authors have completed the ICMJE uniform disclosure form (available at https://qims.amegroups.com/article/view/10.21037/qims-23-843/coif). S.D. and J.D. are employees of Philips Healthcare, the manufacturer of the CT system used in this study. The other authors have no conflicts of interest to declare.

Ethical Statement: The authors are accountable for all aspects of the work in ensuring that questions related to the accuracy or integrity of any part of the work are appropriately investigated and resolved. This retrospective study was conducted in accordance with the Declaration of Helsinki (as revised in 2013) and approved by the Institutional Review Board of The First Affiliated Hospital of Zhengzhou University (No. 2022-KY-1396). The requirement for individual consent for this retrospective analysis was waived.

References

1. Wei S, Li C, Li M, Xiong Y, Jiang Y, Sun H, Qiu B,

Lin CJ, Wang J. Radioactive Iodine-125 in Tumor Therapy: Advances and Future Directions. Front Oncol 2021;11:717180.
2. Cao Q, Wang H, Meng N, Jiang Y, Jiang P, Gao Y, Tian S, Liu C, Yang R, Wang J, Zhang K. CT-guidance interstitial (125)Iodine seed brachytherapy as a salvage therapy for recurrent spinal primary tumors. Radiat Oncol 2014;9:301.
3. Yang Q, Peng S, Wu J, Ban X, He M, Xie C, Zhang R. Spectral CT with monochromatic imaging and metal artifacts reduction software for artifacts reduction of ^{125}I radioactive seeds in liver brachytherapy. Jpn J Radiol 2015;33:694-705.
4. Liu J, Wang W, Zhao X, Shen Z, Shao W, Wang X, Li L, Wang B. The value of spectral imaging to reduce artefacts in the body after (125) I seed implantation. J Med Imaging Radiat Oncol 2016;60:643-9.
5. Tanaka N, Yorozu A, Kikuchi T, Higashide S, Kojima S, Ohashi T, Katayama N, Nakamura K, Saito S, Dokiya T, Fukushima M; J-POPS Study Group. Genitourinary toxicity after permanent iodine-125 seed implantation: The nationwide Japanese prostate cancer outcome study of permanent iodine-125 seed implantation (J-POPS). Brachytherapy 2019;18:484-92.
6. Ji Z, Jiang Y, Tian S, Guo F, Peng R, Xu F, Sun H, Fan J, Wang J. The Effectiveness and Prognostic Factors of CT-Guided Radioactive I-125 Seed Implantation for the Treatment of Recurrent Head and Neck Cancer After External Beam Radiation Therapy. Int J Radiat Oncol Biol Phys 2019;103:638-45.
7. Jiang Y, Zhen P, Dai J, Li Y, Liu S, Xu J, Wang Y, Tian S, Cui Y, Ji Z, Guo F, Qiu B, Sun H, Fan J, Wang J. Long-Term Safety and Efficacy of CT-Guided I(125) Radioactive Seed Implantation as a Salvage Therapy for Recurrent Head and Neck Squamous Carcinoma: A Multicenter Retrospective Study. Front Oncol 2021;11:645077.
8. Wanderley VA, Vasconcelos KF, Leite AF, Oliveira ML, Jacobs R. Dentomaxillofacial CBCT: Clinical Challenges for Indication-oriented Imaging. Semin Musculoskelet Radiol 2020;24:479-87.
9. Wellenberg RHH, Hakvoort ET, Slump CH, Boomsma MF, Maas M, Streekstra GJ. Metal artifact reduction techniques in musculoskeletal CT-imaging. Eur J Radiol 2018;107:60-9.
10. Große Hokamp N, Hellerbach A, Gierich A, Jordan DW, Visser-Vandewalle V, Maintz D, Haneder S. Reduction of Artifacts Caused by Deep Brain Stimulating Electrodes in Cranial Computed Tomography Imaging by Means of Virtual Monoenergetic Images, Metal Artifact Reduction Algorithms, and Their Combination. Invest Radiol 2018;53:424-31.
11. Zhang K, Han Q, Xu X, Jiang H, Ma L, Zhang Y, Yang K, Chen B, Wang J. Metal artifact reduction of orthopedics metal artifact reduction algorithm in total hip and knee arthroplasty. Medicine (Baltimore) 2020;99:e19268.
12. Lell MM, Wildberger JE, Alkadhi H, Damilakis J, Kachelriess M. Evolution in Computed Tomography: The Battle for Speed and Dose. Invest Radiol 2015;50:629-44.
13. Park J, Kim SH, Han JK. Combined application of virtual monoenergetic high keV images and the orthopedic metal artifact reduction algorithm (O-MAR): effect on image quality. Abdom Radiol (NY) 2019;44:756-65.
14. Selles M, Stuivenberg VH, Wellenberg RHH, van de Riet L, Nijholt IM, van Osch JAC, van Hamersvelt RW, Leiner T, Boomsma MF. Quantitative analysis of metal artifact reduction in total hip arthroplasty using virtual monochromatic imaging and orthopedic metal artifact reduction, a phantom study. Insights Imaging 2021;12:171.
15. Choo HJ, Lee SJ, Kim DW, Lee YJ, Baek JW, Han JY, Heo YJ. Comparison of the Quality of Various Polychromatic and Monochromatic Dual-Energy CT Images with or without a Metal Artifact Reduction Algorithm to Evaluate Total Knee Arthroplasty. Korean J Radiol 2021;22:1341-51.
16. Neuhaus V, Grosse Hokamp N, Zopfs D, Laukamp K, Lennartz S, Abdullayev N, Maintz D, Borggrefe J. Reducing artifacts from total hip replacements in dual layer detector CT: Combination of virtual monoenergetic images and orthopedic metal artifact reduction. Eur J Radiol 2019;111:14-20.
17. Hu Y, Pan S, Zhao X, Guo W, He M, Guo Q. Value and Clinical Application of Orthopedic Metal Artifact Reduction Algorithm in CT Scans after Orthopedic Metal Implantation. Korean J Radiol 2017;18:526-35.
18. Sellerer T, Noël PB, Patino M, Parakh A, Ehn S, Zeiter S, Holz JA, Hammel J, Fingerle AA, Pfeiffer F, Maintz D, Rummeny EJ, Muenzel D, Sahani DV. Dual-energy CT: a phantom comparison of different platforms for abdominal imaging. Eur Radiol 2018;28:2745-55.
19. Huang JY, Kerns JR, Nute JL, Liu X, Balter PA, Stingo FC, Followill DS, Mirkovic D, Howell RM, Kry SF. An evaluation of three commercially available metal artifact reduction methods for CT imaging. Phys Med Biol 2015;60:1047-67.
20. Zheng H, Yang M, Jia Y, Zhang L, Sun X, Zhang Y, Nie Z, Wu H, Zhang X, Lei Z, Jing W. A Novel Subtraction Method to Reduce Metal Artifacts of Cerebral Aneurysm

Embolism Coils. Clin Neuroradiol 2022;32:687-94.
21. Laukamp KR, Zopfs D, Lennartz S, Pennig L, Maintz D, Borggrefe J, Große Hokamp N. Metal artifacts in patients with large dental implants and bridges: combination of metal artifact reduction algorithms and virtual monoenergetic images provides an approach to handle even strongest artifacts. Eur Radiol 2019;29:4228-38.
22. Schmidt AMA, Grunz JP, Petritsch B, Gruschwitz P, Knarr J, Huflage H, Bley TA, Kosmala A. Combination of Iterative Metal Artifact Reduction and Virtual Monoenergetic Reconstruction Using Split-Filter Dual-Energy CT in Patients With Dental Artifact on Head and Neck CT. AJR Am J Roentgenol 2022;218:716-27.
23. Sunwoo L, Park SW, Rhim JH, Kang Y, Chung YS, Son YJ, Kim SC. Metal Artifact Reduction for Orthopedic Implants: Brain CT Angiography in Patients with Intracranial Metallic Implants. J Korean Med Sci 2018;33:e158.
24. Zopfs D, Lennartz S, Pennig L, Glauner A, Abdullayev N, Bremm J, Große Hokamp N, Persigehl T, Kabbasch C, Borggrefe J, Laukamp KR. Virtual monoenergetic images and post-processing algorithms effectively reduce CT artifacts from intracranial aneurysm treatment. Sci Rep 2020;10:6629.

Cite this article as: Zhou Y, Lei L, Wang Z, Cao W, Qin M, Dong S, Dang J, Zhou Z. Utility of spectral CT with orthopedic metal artifact reduction algorithms for ^{125}I seeds implantation in mediastinal and hepatic tumors. Quant Imaging Med Surg 2024;14(1):698-710. doi: 10.21037/qims-23-843